

# Iron self-diffusion in B2-FeRh thin film

D.G. Merkel<sup>a,b,\*</sup>, S. Sajti<sup>a</sup>, L. Deák<sup>a</sup>, G. Hegedűs<sup>a</sup>, Z.E. Horváth<sup>b</sup>, A. Lengyel<sup>a</sup>

<sup>a</sup> Wigner Research Centre for Physics, Konkoly-Thege Miklós út 29-33, Budapest, 1121, Hungary

<sup>b</sup> Centre for Energy Research, Konkoly-Thege Miklós út 29-33, Budapest, 1121, Hungary

## ARTICLE INFO

Handling Editor: Prof. L.G. Hultman

## ABSTRACT

Iron-rhodium thin films are in the center of scientific interest due to their great potential in spintronic, energy harvesting and other forthcoming applications. The structural stability of these materials in industrial applications relies heavily on their ability to withstand temperature variations, therefore it is crucial to gain a thorough understanding of the diffusion processes induced by temperature. To investigate the self-diffusion of iron in FeRh, an isotope-periodic multilayer structure of [<sup>56</sup>Fe<sub>50.5</sub>Rh<sub>49.5</sub>(63 Å)/<sup>57</sup>Fe<sub>51.5</sub>Rh<sub>48.5</sub>(46 Å)]<sub>10</sub> was prepared by molecular beam epitaxy. By using neutron reflectivity technique, which is capable of detecting atomic-scale diffusion lengths, we determined the pre-exponent factor and activation energy as  $D_0 = (1.19 \pm 0.5) \times 10^{-16} \text{ m}^2\text{s}^{-1}$  and  $E_a = (1.00 \pm 0.03) \text{ eV}$  respectively.

## 1. Introduction

FeRh intermetallic alloy exhibits a first-order phase transition from an antiferromagnetic (AFM) state to a ferromagnetic (FM) state near room temperature [1–8], making it a prime candidate for spintronic applications [9–23]. Furthermore, FeRh has also been found to exhibit giant magnetocaloric effect, magnetostriction, and Thomson effect, which make it a versatile material for magnetic refrigeration, sensing, and energy harvesting applications [24–29].

The potential application of these materials in industrial settings relies heavily on their structural stability at different temperatures. Atomic diffusion influences processes such as dislocation movement, vacancy formation, and diffusion-controlled phase changes, all of which contribute to the alloy's strength, ductility, and other mechanical characteristics. Consequently, it is crucial to gain a comprehensive understanding of the atomic-scale behavior and performance of alloys, enabling to optimize their properties for specific applications and improve their overall reliability and functionality [30–32].

Studying self-diffusion at the atomic scale poses significant challenges. While the radio-tracer technique can provide insights into mesoscopic and macroscopic diffusion [33], and X-ray reflectometry is capable of measuring small diffusivity, the study of self-diffusion itself is not feasible with these techniques [34]. Consequently, specialized methods that are sensitive to isotopes are necessary, such as synchrotron Mössbauer reflectometry or neutron reflectometry, which employ isotope modulated multilayers to track diffusion processes at

subnanometer scales [35–39].

In our study, we employ FeRh multilayer thin films comprising alternating layers of <sup>57</sup>Fe isotope and natural Fe. By utilizing the isotope-sensitive neutron reflectivity technique, we are able to track the diffusion of iron within the sample. This allows us to investigate the pre-exponential factor and activation energy associated with iron self-diffusion in FeRh.

## 2. Experimental

Chemically homogenous but isotope periodic multilayer system consisting of [<sup>56</sup>Fe<sub>50.5</sub>Rh<sub>49.5</sub>(63 Å)/<sup>57</sup>Fe<sub>51.5</sub>Rh<sub>48.5</sub>(46 Å)] bilayer sequences of ten times was created on a MgO(100) substrate by using molecular beam epitaxy (MBE) technique (<sup>56</sup>Fe stands for Fe of natural isotopic abundance) (Fig. 1). Before the deposition process, the substrate underwent a cleaning process by immersing it in an ultrasonic bath filled with ethanol, followed by a 630 °C, 30 min baking under ultrahigh vacuum (UHV) conditions. The film was prepared through co-evaporation using electron gun for <sup>56</sup>Fe and Rh, and effusion cell for <sup>57</sup>Fe evaporation (isotopic enrichment 95%), with growing rate of 0.0248 Å/s, 0.0440 Å/s and 0.0248 Å/s respectively. To ensure better homogeneity, the substrate was rotated continuously during sample preparation. The substrate temperature was held at 200 °C and the pressure never exceeded  $1.2 \times 10^{-8} \text{ mbar}$ . The epitaxial growth was monitored by an in-situ reflection high-energy electron diffraction (RHEED). The transmission electron microscopy, the Rutherford

\* Corresponding author. Wigner Research Centre for Physics, Konkoly-Thege Miklós út 29-33, Budapest, 1121, Hungary.

E-mail address: [merkel.daniel@wigner.hu](mailto:merkel.daniel@wigner.hu) (D.G. Merkel).

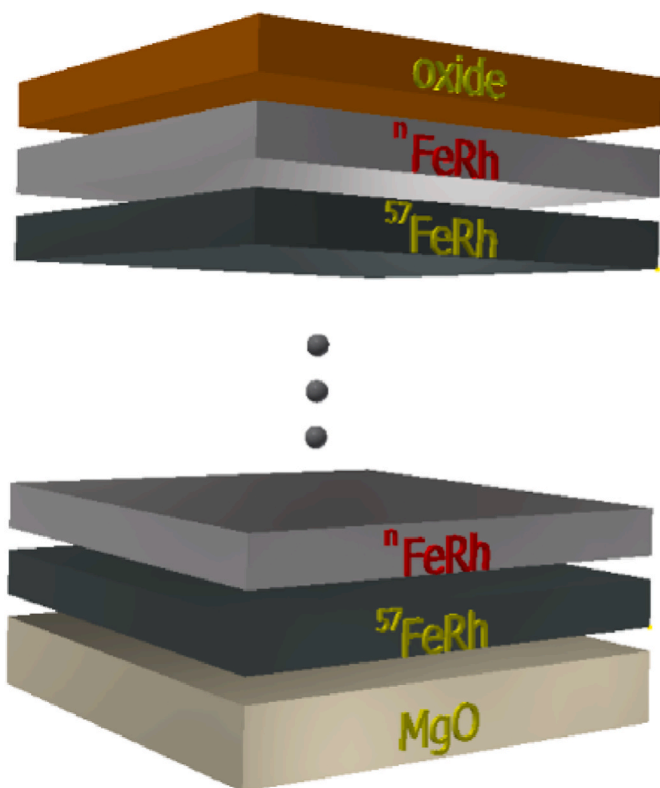


**Fig. 1.** Layer structure of  $[{}^n\text{FeRh}/{}^{57}\text{FeRh}]_{10}$  isotope periodic multilayer structure.

backscattering spectrometry and the neutron reflectivity characterizations of the sample can be found in Ref 14. To achieve B2 ordering, the sample underwent annealing at 300 °C for 60 min, which was subsequently confirmed through the use of X-ray diffraction (XRD). From this point, this state of sample will be referred as the initial sample.

The XRD pattern was obtained by using a Bruker® D8 Discover type diffractometer with Cu K $\alpha$  radiation ( $\lambda = 1.5418$  Å). To enhance the parallelism of the beam and reduce beam divergence, 0.6 mm slits were installed at the source and detector sides, while a 90-degree rotated Soller slit was placed between the sample and the detector-side slit. In addition, a secondary monochromator was used at the detector side to improve the signal-to-noise ratio of the results.

The original 20 mm  $\times$  20 mm sample was divided into multiple pieces, each of which underwent individual annealing under a high vacuum condition of approximately  $10^{-7}$  mbar. The temperatures for annealing and their respective durations are outlined in Table 1.

The investigation of temperature-induced interlayer mixing was conducted using unpolarized neutron reflectometry (NR) at the GINA neutron reflectometer located at the Budapest Neutron Centre. [28, 29]. A 4.61 Å wavelength monochromatic beam was generated by a pyrolytic graphite monochromator, while higher harmonics were eliminated by using a liquid nitrogen cooled Be-filter. The neutron beam was collimated by two slits to a 0.6 mm size in the scattering direction, and the

sample was maintained at room temperature throughout the experiment. Specularly reflected neutrons were detected by a position-sensitive detector, and the reflectivities were assessed by using the Fit-Suite program40.

### 3. Results and discussion

The confirmation of B2 structure of FeRh was done by using theta-2theta X-ray diffraction technique (Fig. 2). The evaluation of the spectrum revealed B2-FeRh phase in the sample with base centered cubic structure (see inner picture of Fig. 2). The XRD pattern exhibit distinct peaks at  $2\theta = 29.75^\circ$ ,  $42.94^\circ$  and  $61.77^\circ$ , which can be associated with the crystallographic planes of B2-FeRh(001), MgO(002), and B2-FeRh(002), respectively [41–43].

In order to analyze and quantify the atomic range self-diffusion of iron, neutron reflectivity measurements were carried out on the initial and the subsequent annealed samples.

A well-established method for extracting diffusion information from reflectivity curves involves monitoring the decrease in height of the isotopic multilayer Bragg peak, normalized to the intensity of the total reflection region [34–45]. However, it should be noted that the intensity of the peak is highly sensitive to slight variations in beam alignments, and it can be affected by overlapping with Kiessig fringes, therefore, the normalization process may introduce some degree of uncertainty [46, 47].

In the recent analysis, the complete reflectivity curve was fitted using a layer model that properly considered the diffusion history of the multilayer. The diffusion-induced interface roughness was incorporated by employing a one-dimensional diffusion profile characterized by the squared diffusion length ( $Dt$ ), where  $D$  represents the diffusion coefficient and  $t$  represents the diffusion time. The diffusion profile was adjusted through  $Dt$  to accurately match the measured reflectivity curves. To approximate the error-function interface profile, a step function was utilized, with the resolution controlled by additional program parameters [46]. The MgO-FeRh (bottom) and FeRh –oxide (top) interfaces were excluded from this procedure. This is reasonable as it has only a small effect on the Bragg-peak, and it was taken into account by changing the roughness of this interface.

Fig. 3b displays the neutron reflectivity curves obtained from the initial sample and the annealed samples at various temperatures: 450 °C, 550 °C, 600 °C, 650 °C (for 90 min), and 750 °C (for 40 min). The red line represents the fitted spectrum using the bilayer diffusion profile shown on the left side of the figure. In Fig. 3c, the profile ranges from 0 to 0.5, indicate the concentration variation of  ${}^{57}\text{Fe}$  in the originally  ${}^{57}\text{FeRh}/{}^n\text{FeRh}$  bilayer. At early stages, the reflectivity spectra features Bragg peaks to the 2nd order due to a distinct bilayer structure, which is

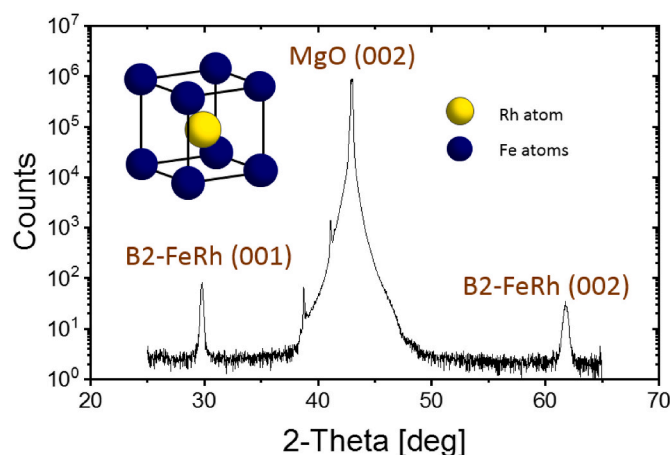


**Fig. 2.** X-ray diffraction pattern of B2-FeRh sample. The inner picture shows the body centered cubic cell of B2 crystal structure.

**Table 1**

The annealing temperatures and times used for the experiment.

Annealing Temp. (°C)	Annealing time (s)
400	2400, 5400
450	2400, 5400
550	2400, 5400
600	2400, 5400
650	2400, 5400
750	2400

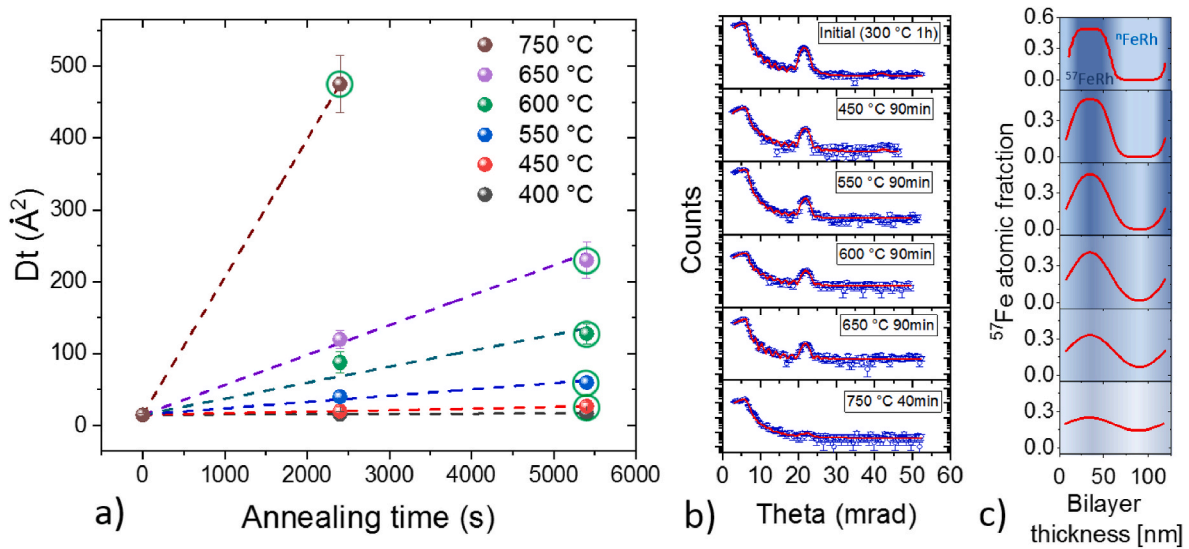


**Fig. 3.** a) The change of squared diffusion lengths ( $Dt$ ) for different temperatures as a function of annealing time. The circles note the data points whose neutron reflectivity curves are shown b) Neutron reflectivity curves taken on initial and on annealed samples at 400 °C, 450 °C, 550 °C, 600 °C, 650 °C with annealing time of 90 min and at 750 °C for 40 min. The symbols represent the measured data, while the red line is the fitted reflectivity curve. c) The extracted  $^{57}\text{Fe}$  diffusion profile is shown, indicating the relative concentration of  $^{57}\text{Fe}$  to  $^{56}\text{Fe}$  in the isotope bilayer.

reflected by the square-like shape of the diffusion profile.

As a consequence of the self-diffusion of iron, the concentration of  $^{57}\text{Fe}$  and  $^{56}\text{Fe}$  tends to reach equilibrium in the neighboring layers, resulting in the gradual disappearance of the isotope multilayer characteristic. This phenomenon is evident in Fig. 3b, where the decay of the Bragg peak becomes more pronounced with increasing annealing temperature, and consequently leads to the emergence of a flattened diffusion profile (Fig. 3c).

The results depicted in Fig. 3a present the  $Dt$  values (squared diffusion length) corresponding to different annealing times and temperatures. The points highlighted with a circle correspond to the demonstrated neutron reflectivity curves. The evaluation reveals that even in the initial sample, there is a noticeable degree of interface mixing, as evidenced by the diffusion length ( $L_d = \sqrt{2Dt}$ ) of 3.87  $\text{\AA}$ . By fitting the obtained  $Dt$  values for each temperature with a linear regression, assuming a constant diffusion coefficient over time, the average diffusion coefficients were determined and shown in Table 2.

The obtained diffusion coefficients are presented in Fig. 4 as an Arrhenius plot. Applying the formula of  $D = D_0 \exp\left(-\frac{E_a}{k_b T}\right)$ , where  $k_b$  represents the Boltzmann constant and  $T$  the temperature, the activation energy ( $E_a$ ) and pre-exponential factor ( $D_0$ ) were determined as  $(1.00 \pm 0.03)$  eV and  $(1.19 \pm 0.5) \times 10^{-16} \text{ m}^2\text{s}^{-1}$  respectively.

Comparing these values to the iron self-diffusion in other binary iron alloys reported in the literature, it can be seen, that the iron self-diffusion observed in the FeRh thin film showcases a consistency with the established values (eg.: in  $\text{Li}_0\text{FePt}$ :  $D_0 = (3.45 \pm 0.44) \times 10^{-13} \text{ m}^2\text{s}^{-1}$ ,  $E_a = (1.65 \pm 0.29)$  eV [43]),  $\text{Fe}_{70}\text{Zr}_{30}$ :  $D_0 = (1.15 \pm 0.03) \times 10^{-17} \text{ m}^2\text{s}^{-1}$ ,  $E_a = (0.42 \pm 0.04)$  eV [36] or in  $\text{Fe}_5\text{Ge}_3$ :  $D_0 = (8.22 \pm 3.8) \times 10^{-18} \text{ m}^2\text{s}^{-1}$ ,  $E_a = (0.28 \pm 0.02)$  eV [48]).

In an effort to elucidate the diffusion mechanism within our system,

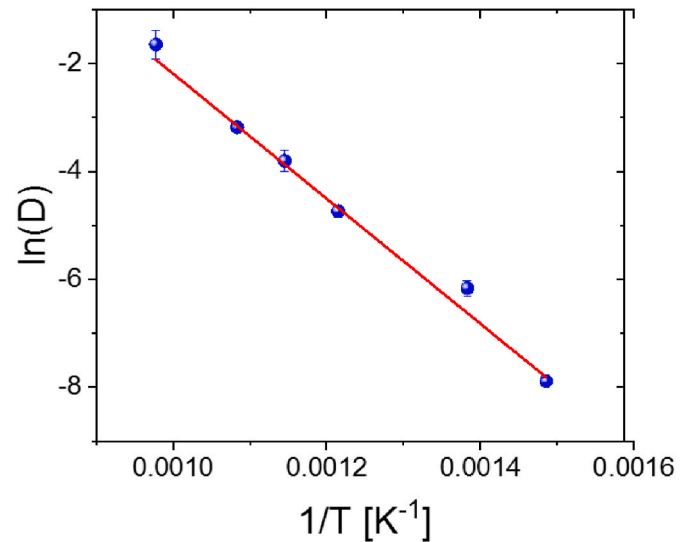


**Fig. 4.** The obtained average diffusion coefficients as a function of annealing temperature.

we aligned our findings with the Harrison diffusion kinetics regimes [49], which most accurately corresponded to our experimental results. In this work three regime A, B and C were defined for bulk, mixed and grain boundary diffusion, respectively. To achieve this, we employed the grain boundary width  $\delta = 0.5$  nm, a commonly accepted value for metals [50], the average grain diameter,  $d = 40.2$  nm, determined from X-ray diffraction B2-FeRh (001) peak (see Fig. 2) using the Scherrer formula [51] and the determined temperature-dependent diffusion coefficient.

In the parameters  $\Lambda$  and  $\alpha$  used by Ref. [52] were plotted in Fig. 5 to identify the regimes. According to this, below 350 °C it is the C regime, where the diffusion takes place only along the grain boundary. In our case a grain of size  $d = 40.2$  nm, crosses at least three isotopic bilayers of thickness 10.9 nm (i.e. 6 interfaces). The models on which the Harrison classification scheme is based were not created for description of such systems, its usability is questionable. The volume of the grain boundaries is only about  $3\delta/d < 4\%$  of the grains, the fast decrease of the Bragg-peak at higher temperatures requires mixing in larger volume, i.e.

**Table 2**

The average diffusion coefficients at different annealing temperatures.

Temperature (°C)	Diffusion coefficient ( $\text{\AA}^2\text{s}^{-1}$ )
450	$0.0021 \pm 0.0003$
550	$0.0088 \pm 0.0010$
600	$0.0223 \pm 0.0043$
650	$0.0416 \pm 0.0020$
750	$0.1917 \pm 0.0500$

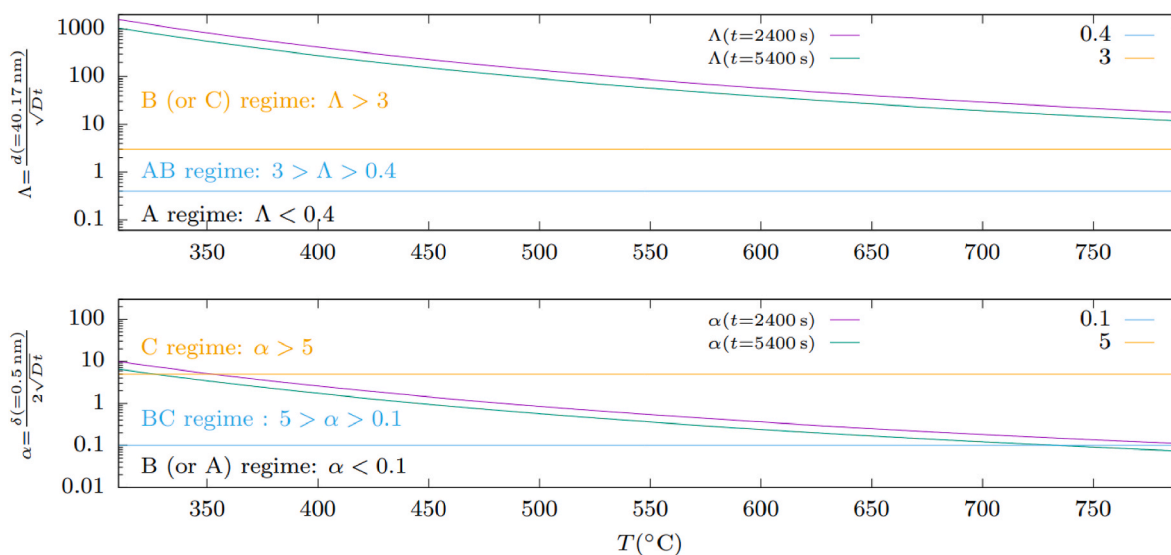


**Fig. 5.** The Harrison diffusion kinetics (type A: volume, B: mixed, C: grain boundary diffusion) regimes relevant to our experiments based on [52]. The regimes are determined by the parameters  $\alpha = \delta / (2\sqrt{Dt})$  and  $\Lambda = d / \sqrt{Dt}$ , where  $\delta$  is the grain boundary width,  $d$  is the grain size (diameter),  $t$  is the annealing time, and  $D$  is temperature dependent bulk diffusion coefficient, which we replaced by the effective diffusion coefficient obtained by fitting.

inside the grains. Considering the aforementioned points, we believe that both volume and grain boundary diffusion occur during the heat treatment, however, the proportion of grain boundaries is relatively minor (less than 4%, therefore, the interlayer mixing most probably occurs through volume diffusion. Nevertheless, it is more appropriate to address our findings as *effective* diffusion in FeRh.

#### 4. Conclusion

The recent work focused on examining the self-diffusion of iron in a thin film of FeRh through the utilization of neutron reflectivity technique. The evaluation process entailed fitting the complete reflectivity curve to a comprehensive layer model, which effectively incorporated the diffusion history of the multilayer system.

A multilayer structure composed of alternating isotopic layers of  $^{56}\text{Fe}_{50.5}\text{Rh}_{49.5}$  (63 Å) and  $^{57}\text{Fe}_{51.5}\text{Rh}_{48.5}$  (46 Å) was deposited by using molecular beam epitaxy technique. The samples underwent annealing procedures at temperatures of 450 °C, 550 °C, 600 °C, 650 °C and 750 °C, for 40 or 90 min. Following each annealing step, the modified  $^{57}\text{Fe}$  self-diffusion profile in the adjacent layers were numerically calculated and for the first time in this system, the pre-exponent factor and activation energy were determined and were found to be  $D_0 = (1.19 \pm 0.5) \times 10^{-16} \text{ m}^2\text{s}^{-1}$  and  $E_a = (1.00 \pm 0.03) \text{ eV}$  respectively.

The results were correlated with Harrison's diffusion kinetics regimes, specifically focusing on regime A for bulk, B for mixed, and C for grain boundary diffusion. This alignment was based on employing a grain boundary width of  $\delta = 0.5 \text{ nm}$ , along with an average grain diameter of  $d = 40.2 \text{ nm}$ . We concluded that both volume and grain boundary diffusion take place during heat treatment. However, the relatively small fraction of grain boundaries (less than 4%) indicates that interlayer mixing predominantly occurs through volume diffusion.

These findings hold significant implications for applications involving iron-rhodium, particularly in terms of ensuring the thermal stability of related devices.

#### CRedit authorship contribution statement

**D.G. Merkel:** Writing – review & editing, Writing – original draft, Visualization, Methodology, Investigation, Formal analysis, Data curation, Conceptualization. **S. Sajti:** Writing – review & editing, Software, Investigation, Formal analysis. **L. Deák:** Writing – review & editing,

Conceptualization. **G. Hegedűs:** Methodology, Investigation. **Z.E. Horváth:** Methodology, Investigation. **A. Lengyel:** Writing – review & editing, Writing – original draft, Visualization, Validation, Methodology, Conceptualization.

#### Declaration of competing interest

The authors declare that they have no known competing financial interests or personal relationships that could have appeared to influence the work reported in this paper.

#### Data availability

Data will be made available on request.

#### Acknowledgement

The authors express their gratitude to Edit Szilágyi for the Rutherford Backscattering Spectrometry calibration for the MBE equipment.

#### References

- [1] R.O. Cherifi, V. Ivanovskaya, L.C. Phillips, A. Zobelli, I.C. Infante, E. Jacquet, V. Garcia, S. Fusil, P.R. Briddon, N. Guiblin, A. Mougín, A.A. Únal, F. Kronast, S. Valencia, B. Dkhil, A. Barthélémy, M. Bibes, *Nat. Mater.* 13 (4) (2014) 345.
- [2] M. Fallot, R. Hocart, *Rev. Sci. Instrum.* 77 (1939) 498.
- [3] A.A. Amirov, V.V. Rodionov, V. Komanicky, V. Latyshev, E. Yu Kaniukov, V. V. Rodionova, *J. Magn. Magn. Mater.* 479 (2019) 287.
- [4] L.C. Phillips, R.O. Cherifi, V. Ivanovskaya, A. Zobelli, I.C. Infante, E. Jacquet, N. Guiblin, A.A. Únal, F. Kronast, B. Dkhil, A. Barthélémy, M. Bibes, S. Valencia, *Sci. Rep.* 5 (2015) 1.
- [5] A. Chirkova, F. Bittner, K. Nenkov, N.V. Baranov, L. Schultz, K. Nielsch, T. G. Woodcock, *Acta Mater.* 131 (2017) 31.
- [6] G. Li, R. Medapalli, J.H. Mentink, R.V. Mikhaylovskiy, T.G.H. Blank, S.K.K. Patel, A.K. Zvezdin, Th Rasing, E.E. Fullerton, A.V. Kimel, *Nat. Commun.* 13 (2022) 2998.
- [7] A.S. Komlev, D.Y. Karpenkov, D.A. Kiselev, T.S. Ilina, A. Chirkova, R.R. Gimaev, T. Usami, T. Taniyama, V.I. Zverev, N.S. Perov, *J. Alloys Compd.* 874 (2021), 159924.
- [8] A. Lengyel, G. Bazsó, A.I. Chumakov, D.L. Nagy, G. Hegedűs, D. Bessas, Z. E. Horváth, N. Nemes, M.A. Gracheva, E. Szilágyi, S. Sajti, D.G. Merkel, *Mater. Sci. Eng. B - Solid State Mater. Adv. Technol.* 285 (2022), 115939.
- [9] F. Pressacco, D. Sangalli, V. Uhlir, D. Kutnyakhov, J.A. Arregi, S.Y. Agustsson, G. Brenner, H. Redlin, M. Heber, D. Vasilyev, J. Demsar, G. Schönhense, M. Gatti, A. Marini, W. Wurth, F. Sirotti, *Nat. Commun.* 12 (1) (2021) 5088.
- [10] G. Nava Antonio, I. Bertelli, B.G. Simon, R. Medapalli, D. Afanasiev, T. van der Sar, *J. Appl. Phys.* 129 (22) (2021), 223904.



- [11] V.I. Zverev, R.R. Gimaev, T. Miyanaga, A.A. Vaulin, A.F. Gubkin, B.B. Kovalev, A. M. dos Santos, E. Lovell, L.F. Cohen, N.A. Zarkevich, J. Magn. Magn Mater. 522 (2021), 167560.
- [12] A.M. Chirkova, K.P. Skokov, Y. Skourski, F. Scheibel, A.Y. Karpenkov, A. S. Volegov, N.V. Baranov, K. Nielsch, L. Schultz, K.-H. Müller, T.G. Woodcock, O. Gutfleisch, Phys. Rev. Mater. 5 (6) (2021), 064412.
- [13] T. Usami, M. Itoh, T. Taniyama, AIP Adv. 11 (4) (2021), 045302.
- [14] D.G. Merkel, A. Lengyel, D.L. Nagy, A. Németh, Zs E. Horváth, Cs Bogdán, M. A. Gracheva, G. Hegedűs, Sz Sajti, Gy Z. Radnóczy, E. Szilágyi, Sci. Rep. 10 (1) (2020), 13923.
- [15] W. Griggs, C. Bull, C.W. Barton, R.A. Griffiths, A.J. Caruana, C.J. Kinane, P. W. Nutter, T. Thomson, Phys. Rev. Mater. 6 (2022), 024403.
- [16] D.G. Merkel, G. Hegedűs, M. Gracheva, A. Deák, L. Illés, A. Németh, F. Maccari, I. Radulov, M. Major, A.I. Chumakov, D. Bessas, D. Lajos Nagy, Zs Zolnai, S. Graning, K. Sajerma, E. Szilágyi, A. Lengyel, ACS Appl. Nano Mater. 5 (4) (2022) 5516.
- [17] S. Zhang, S. Xia, Q. Li, B. Yang, J. Li, Q. Cao, D. Wang, R. Liu, Y. Du, Appl. Phys. Lett. 118 (14) (2021), 142401.
- [18] M.J. Jiménez, A.B. Schvval, G.F. Cabeza, J. Magn. Magn Mater. 526 (2021), 167727.
- [19] Y. Wang, M.M. Decker, T.N.G. Meier, X. Chen, C. Song, T. Grünbaum, W. Zhao, J. Zhang, L. Chen, C.H. Back, Nat. Commun. 11 (1) (2020) 275.
- [20] I. Fina, N. Dix, E. Menéndez, A. Crespi, M. Foerster, L. Aballe, F. Sánchez, J. Fontcuberta, ACS Appl. Mater. Interfaces 12 (13) (2020), 15389.
- [21] C.D. Cress, D. Wickramaratne, M.R. Rosenberger, Z. Hennighausen, P.G. Callahan, S.W. LaGasse, N. Bernstein, O.M. van 't Erve, B.T. Jonker, S.B. Qadri, J. C. Prestigiacomo, M. Currie, I.I. Mazin, S.P. Bennett, ACS Appl. Mater. Interfaces 13 (1) (2021) 836.
- [22] R. Nadarajah, S. Tahir, J. Landers, D. Koch, A.S. Semisalova, J. Wiemeler, A. El-Zoka, S.-H. Kim, D. Utzat, R. Möller, B. Gault, H. Wende, M. Farle, B. Gökce, Nanomaterials 10 (2020) 2362.
- [23] J.R. Massey, K. Matsumoto, M. Strungaru, R.C. Temple, T. Higo, K. Kondou, R.F. L. Evans, G. Burnell, R.W. Chantrell, Y. Otani, C.H. Marrows, Phys. Rev. Mater. 4 (2020), 024403.
- [24] R. Modak, M. Murata, D. Hou, A. Miura, R. Iguchi, B. Xu, R. Guo, J. Shiomi, Y. Sakuraba, K.-i. Uchida, Appl. Phys. Rev. 9 (2022), 011414.
- [25] K. Qiao, Y. Liang, H. Zhang, F. Hu, Z. Yu, Y. Long, J. Wang, J. Sun, T. Zhao, B. Shen, J. Alloys Compd. 907 (2022), 164574.
- [26] R.R. Gimaev, A.A. Vaulin, A.F. Gubkin, V.I. Zverev, Phys. Met. Metallogr. 121 (9) (2020) 823.
- [27] A.S. Komlev, V.I. Zverev, Chapter 14 - magnetocaloric effect for medical applications, Editor(s): Alexander M. Tishin, in: Woodhead Publishing Series in Electronic and Optical Materials, Magnetic Materials and Technologies for Medical Applications, Woodhead Publishing, 2022.
- [28] A. Amirov, Chapter 15 - multiferroic, magnetic, and magnetoelectric nanomaterials for medical applications, Editor(s): alexander M. Tishin, in: Woodhead Publishing Series in Electronic and Optical Materials, Magnetic Materials and Technologies for Medical Applications, Woodhead Publishing, 2022.
- [29] L. Casillas-Trujillo, R. Armiento, B. Alling, Phys. Rev. Mater. 5 (2021), 034417.
- [30] F. Liu, L. Fang, Z. Li, Y. Tan, J. Wang, X. He, G. Xu, Y. Ouyang, X. Tao, Vacuum 216 (2023), 112109.
- [31] T. Zhou, Q. Liu, X. Lu, W. Pan, R. Liu, G. Xie, M. Li, C. Wang, Vacuum 212 (2023), 112022.
- [32] Y. Wei, L. Zhu, Y. Li, Y. Chen, Bingbing Guo, Vacuum 213 (2023), 112167.
- [33] H. Mehrer, in: P. Heitjans, J. Kärger (Eds.), Diffusion in Condensed Matter, springer, New York, 2005, p. 3.
- [34] W.-H. Wang, H.Y. Bai, M. Zhang, J.H. Zhao, X.Y. Zhang, W.K. Wang, Phys. Rev. B 59 (1999) 10811–10822.
- [35] M. Gupta, A. Gupta, R. Gupta, T. Gutberlet, J. Phase Equilibria Diffus. 26 (2005) 458.
- [36] M. Rennerhofer, B. Sepiol, M. Sladeczek, D. Kmiec, S. Stankov, G. Vogl, M. Kozłowski, R. Kozubski, A. Vantomme, J. Meersschant, R. Rüffer, A. Gupta, Phys. Rev. B 74 (2006), 104301.
- [37] A. Gupta, S. Chakravarty, P. Rajput, M. Gupta and R. Rüffer, Hyp, Int 182 (2008) 23–30.
- [38] A. Gupta, M. Gupta, U. Pietsch, S. Ayachit, S. Rajagopalan, A.K. Balamurgan, A. K. Tyagi, J. Non-Cryst. Solid. 343 (2004) 39.
- [39] H. Schmidt, E. Hüger, S. Chakravarty, J. Stahn, T. Gutberlet, U. Tietze, Dieter Lott, Adv. Eng. Mater. 11 (2009) 446.
- [40] Sz Sajti, H. Spiering, <http://www.fs.kfki.hu>.
- [41] S. Jekal, S.H. Rhim, S.C. Hong, W. Son, A.B. Shick, Surface-termination-dependent magnetism and strong perpendicular magnetocrystalline anisotropy of an FeRh (001) thin film, Phys. Rev. B 92 (2015), 064410.
- [42] R.Y. Gu, V.P. Antropov, Dominance of the spin-wave contribution to the magnetic phase transition in FeRh, Phys. Rev. B 72 (2005), 012403.
- [43] U. Aschauer, R. Braddell, S.A. Brechbühl, P.M. Derlet, N.A. Spaldin, Strain-induced structural instability in FeRh, Phys. Rev. B 94 (2016), 014109.
- [44] M. Rennerhofer, B. Sepiol, M. Sladeczek, D. Kmiec, S. Stankov, G. Vogl, M. Kozłowski, R. Kozubski, A. Vantomme, J. Meersschant, R. Rüffer, A. Gupta, Phys. Rev. B 74 (2006), 104301.
- [45] M. Swain, S. Singh, S. Basu, D. Bhattacharya, R.B. Tokas, M. Gupta, J. Alloys Compd. 631 (2015) 46.
- [46] M.A. Andreeva, N.G. Monina, S. Stankov, Moscow Univ. Phys. Bull. 63 (2) (2008) 132–136.
- [47] D.G. Merkel, S. Sajti, C. Fetzter, J. Major, M. Major, R. Rüffer, A. Rühm, S. Stankov, F. Tanczikó, L. Bottyán, J. Phys. Conf. 211 (2010), 012029.
- [48] D.G. Merkel, A. Lengyel, G. Hegedűs, Cs Bogdán, Z.E. Horváth, E. Szilágyi, Mater. Res. Express 6 (2019), 086413.
- [49] L.G. Harrison, Trans. Faraday Soc. 57 (1961) 1191.
- [50] I. Kaur, Y. Mishin, W. Gust, Fundamentals of Grain and Interphase Boundary Diffusion, Wiley, 1995.
- [51] A.L. Patterson, Phys. Rev. 56 (1939) 978.
- [52] I.V. Belova, G.E. Murch, T. Fiedler, Defect Diffusion Forum 309–310 (2011) 9.